Composite Structures 316 (2023) 117013

Contents lists available at ScienceDirect

Composite Structures

journal homepage: www.elsevier.com/locate/compstruct

Direct and inverse cohesive law identification of hardwood bonded joints with 1C-PUR adhesive using DCB test

A. Majano-Majano [a], A.J. Lara-Bocanegra [a], F. Pereira [b], J. Xavier [c,d,*], J. Morais [b], M.F.S.F. de Moura [e]

[a] Department of Building Structures and Physics, ETS Architecture, Universidad Politécnica de Madrid, Avda Juan de Herrera 4, 28040 Madrid, Spain
[b] CITAB, School of Science and Technology, University of Trás-os-Montes e Alto Douro, 5001-801, Vila Real Portugal
[c] UNIDEMI, Department of Mechanical and Industrial Engineering, NOVA School of Science and Technology, Universidade NOVA de Lisboa, 2829-516 Caparica, Portugal
[d] Intelligent Systems Associate Laboratory (LASI), 4800-058, Guimarães, Portugal
[e] Faculdade de Engenharia da Universidade do Porto, Departamento de Engenharia Mecânica, Rua Dr. Roberto Frias, Porto, 4200-465, Portugal

ARTICLE INFO

Keywords:
Mode I fracture
Cohesive law
Double cantilever beam
Wood
Eucalyptus globulus
Digital image correlation

ABSTRACT

Fracture characterisation under mode I loading of *Eucalyptus globulus* Labill. bonded joints with one-component polyurethane adhesive (1C-PUR) is addressed in this work. The objective is to estimate the cohesive law representative of the fracture behaviour of these joints. A direct and two inverse procedures were employed to determine the softening laws. The direct method is based on local measurement of crack tip displacements using digital image correlation in the course of Double Cantilever Beam (DCB) tests, while the inverse methods rely on load–displacement data and on load-crack tip opening displacement relations by finite element modelling. It was verified that consistent results can be obtained from the three methodologies leading to the conclusion that the classical inverse procedure is the most appealing one owing to its simplicity.

1. Introduction

Engineered wood products (EWPs) commonly used in structures, such as glued laminated timber (GLT), cross-laminated timber (CLT) or laminated veneer lumber (LVL), have originally been developed with softwood and are today mostly manufactured with these species. However, due to the increase of hardwood forest areas in Europe as a result of environmental policies, research related to the development and application of EWPs made from hardwoods has become a field of growing attention [1], leading to the emergence of innovative products with mechanical performance superior to those made from softwoods, such as GLT from chestnut, oak, beech or meranti [2], or LVL from beech [3].

A hardwood of great interest due to its high mechanical properties and fast growth is *Eucalyptus globulus* (also known as southern blue gum). It is a temperate hardwood widespread in southern Europe (mainly in the Iberian Peninsula) [4], Australia and South America. In Europe it is assigned strength class D40 for structural use [5], making it, along with beech and ash, one of the three species growing in Europe with the highest mechanical performance. Although its common use has been pulp production, in recent years there is increasing industrial and institutional interest in the development of higher value-added EWPs (*e.g.*, [6–10]) and their applications [11–13].

Multiple adhesives can currently be used in the manufacture of the most common EWPs (GLT and CLT), such as resorcinol-formaldehyde (RF), phenol resorcinol-formaldehyde (PRF), urea-formaldehyde (UF), melamine urea-formaldehyde (MUF), emulsion polymer isocyanate (EPI) or one component polyurethane (1C-PUR). The latter is experiencing significant growth in the use of structural timber gluing due to the absence of formaldehyde and the advantages it offers during the manufacturing process (no mixing and fast curing at room temperature) [14]. Several studies have analysed its potential when used with hardwoods (*e.g.*, [15,16]) resulting in some national EWP approvals [17,18]. Furthermore, research with *Eucalyptus globulus* L. has brought out the possibility of using 1C-PUR adhesives for the manufacture of EWPs [19,20], whose very high mechanical performance has been demonstrated in recent works by the authors [21,22].

Ensuring the quality of the wood bonded joint is of utmost importance for the safety and durability of structures using glued laminated

* Corresponding author at: UNIDEMI, Department of Mechanical and Industrial Engineering, NOVA School of Science and Technology, Universidade NOVA de Lisboa, 2829-516 Caparica, Portugal.
E-mail addresses: almudena.majano@upm.es (A. Majano-Majano), antoniojose.lara@upm.es (A.J. Lara-Bocanegra), famp@utad.pt (F. Pereira), jmc.xavier@fct.unl.pt (J. Xavier), jmorais@utad.pt (J. Morais), mfmoura@fe.up.pt (M.F.S.F.d. Moura).

https://doi.org/10.1016/j.compstruct.2023.117013
Received 31 October 2022; Received in revised form 25 February 2023; Accepted 4 April 2023
Available online 10 April 2023
0263-8223/© 2023 The Authors. Published by Elsevier Ltd. This is an open access article under the CC BY-NC-ND license (http://creativecommons.org/licenses/by-nc-nd/4.0/).

products. Several tests are available to assess the quality of the bond line, such as the block shear test [23] or the tensile shear test [24]. A large amount of wood failure indicate that its local strength is lower than that of the adhesive and therefore the bonding properties of the joint are considered sufficient. However, no information on the adhesive bond properties is obtained from such procedures [25].

Fracture mechanics-based methods are becoming increasingly common to evaluate adhesive bond properties in terms of fracture energy. In this context, the development of numerical tools addressing the fracture behaviour acquire special relevancy. This is the case of cohesive zone modelling, which combine stress-based criteria to identify damage initiation and fracture mechanics concepts to address damage growth. These models are based on the cohesive law (CL) that mimics a softening relationship between tractions and crack opening displacements. The determination of the appropriate CL shape representative of the bonded assembly is therefore a crucial aspect [26–29]. Two main approaches are commonly used: the direct and the inverse methods.

The direct method is based on the relationship between the strain energy release rate needed to initiate and propagate the crack under the corresponding loading mode (G_{I} for mode I) and the local crack tip opening displacements (CTOD) (w_{I}) measured experimentally in the course of the test. One of the most widely used experimental methods for mode I fracture characterisation of wood bonded joints is the Double Cantilever Beam (DCB) test (*e.g.*, [30–33]). G_{I} is therefore an important property of the adhesive bond and can be derived by different compliance-based data reduction methods. The direct procedure is frequently considered the most rigorous, although some difficulties can be pointed. In fact, the measurement of the w_{I} requires special and sophisticated equipment (*e.g.*, digital image correlation), data smoothing and curve fitting of the $G_{\mathrm{I}} = f(w_{\mathrm{I}})$ correlation for suitable differentiation to give rise to the cohesive law [34–38]. All these operations influence the ensuing cohesive law.

The inverse procedure usually lies on optimization algorithms associated with finite element analysis, aiming to minimize the difference between the numerical and experimental responses by iterative alteration of the cohesive law parameters. Some authors have addressed the CL determination using the classical inverse procedure based on global structural response, i.e., the load–displacement data ($P-\delta$) [36,39–41]. The identification of the cohesive parameters was achieved by iteratively fitting the numerical $P-\delta$ curve with the experimental one. Although these methods based on structural global response provide satisfactory results, the uniqueness of the obtained CZ laws and its validity at local level is questionable. In alternative, inverse procedures including global and local data can be applied to minimize such difficulties [42–45]. In these cases, parameters like CTOD or full-field data of the displacement in the vicinity of the crack tip are used to correlate with a global parameter, as is the case of applied load.

Knowledge about the mechanical behaviour of adhesive bonded joints with hardwoods is necessary to increase their applicability. In previous work by the authors, the fracture properties in mode I loading of *E. globulus* bonded joints have been determined by direct method, with the CL fitted to a logistic function [46].

In the present work, three approaches are analysed and compared for the first time in the context of the CL identification in mode I of *E. globulus* bonded joints with 1C-PUR adhesive: a direct experimental method implemented by measuring the CTOD using Digital Image Correlation (DIC) from DCB tests and fitting the CL to spline functions; and two inverse procedures, one of them considering the load and displacement (δ) data (Global based method), and the other including the local measurement of the crack tip opening displacements (w) measured by DIC combined with the applied load (Global–Local based method). In both cases, an optimization strategy is followed aiming to minimize the differences between the numerical and the experimental $P-\delta$ and $P-w$ curves, respectively, applying the algorithm developed by the authors in [47], which has never been applied to wood bonded joints before. In all cases, the Compliance Based Beam Method (CBBM) was applied as data reduction scheme to determine the evolution of G_{I}, which is based on an equivalent crack concept that has the advantage of not requiring crack length monitoring during propagation.

2. Experimental work

2.1. Specimen preparation

For the experimental study, ten Double Cantilever Beam (DCB) specimens were prepared with the geometry shown in Fig. 1, consisting of two matched timber elements bonded together. The dimensions were $L_1 = 250$ mm, $L = 240$ mm, $2h = 20$ mm, $B = 20$ mm and $t = 0.1$ mm. A mid-height pre-cracked surface of initial length $a_0 = 100$ mm was performed by means of a thin Teflon film in the bonding operation, which reproduced the conditions of a real crack.

Spanish *Eucalyptus globulus* Labill (also known as southern blue gum) from Galicia region was chosen for the adherends, which were cut out from defect free boards. These raw boards had previously been subjected to edgewise bending tests under four-point loading according to [48] to evaluate their static longitudinal modulus of elasticity (E_{L}), giving an average value of 19640 MPa. The average density of the boards determined for a reference moisture content of 12 % was $\rho = 793\ \mathrm{kg\,m^{-3}}$. Other reference material properties of the species to be considered for the present work were taken from [49], who reported mean values of radial modulus of elasticity (E_{R}) and shear modulus of elasticity in the LR plane (G_{LR}) of 1820 MPa and 1926 MPa, respectively, derived from eucalyptus wood with the same origin and similar density to that used here. The two eucalyptus adherends composing the DCB were oriented according to the RL crack propagation system (radial direction normal to the crack plane and longitudinal crack propagation direction).

A structural adhesive, one-component polyurethane (1C-PUR) adhesive type I, PURBOND® HB S109, was used to bond the eucalyptus adherends. It shows important advantages, such as fast curing at room temperature, absence of formaldehyde and solvents, invisible bonding joint appearance, and not requiring mixing. This adhesive contains isocyanate pre-polymer and has a Brookfield viscosity of about 20000 mPa s and a density of approximately 1100 $\mathrm{kg\,m^{-3}}$.

The bonding process was carried out in compliance with the requirements of the adhesive manufacturer. The adhesive was applied manually on one side with an application weight of 200 $\mathrm{g/m^2}$ (Fig. 2(a)).

The coated surfaces were gradually pressed together immediately after the application of the adhesive using an Instron® 1125 testing machine until a target end pressure of 0.8 MPa was reached (four DCB specimens were subjected to pressure at the same time, see Fig. 2(b)). This pressure was then held for 25 min. The final bond strength was attained after approximately 12 h.

2.2. Experimental set-up

The DCB fracture tests were carried out at room temperature using a conventional Instron® 1125 testing machine equipped with a load cell of 5 kN maximum capacity and 50 $\mathrm{N\,V^{-1}}$ gain setting (Fig. 3). The load was applied perpendicular to the pre-cracked surface through a pair of symmetrical pins inserted into two 3 mm diameter holes drilled 10 mm from the end of the specimens, resulting in a mode I fracture along the $L-a_0$ extension shown in Fig. 1. The crosshead displacement rate was set at 3 $\mathrm{mm\,min^{-1}}$. The applied load (P) and the crosshead displacement of the testing machine (δ) were recorded during each test.

The DCB test was coupled with the optical metrology ARAMIS DIC-2D by GOM [50], allowing full-field measurement of displacements at the crack tip area of the specimen during the test. This is a non-contact measuring system that applies the principles of digital image correlation. It consists of a charge coupled device camera (8-bit Baumer Optronic FWX20 model) with a telecentric lens of 0.243 ± 3 % magnification, 29.3 × 22.1 $\mathrm{mm^2}$ field of view and 11 mm field depth, mounted on a translation stage for fine alignment of the optical axis with respect to the target surface. The specimens are illuminated by two cold light sources Raylux 25 white-light LED incorporated in the measuring device. A thin black and white speckle pattern was applied

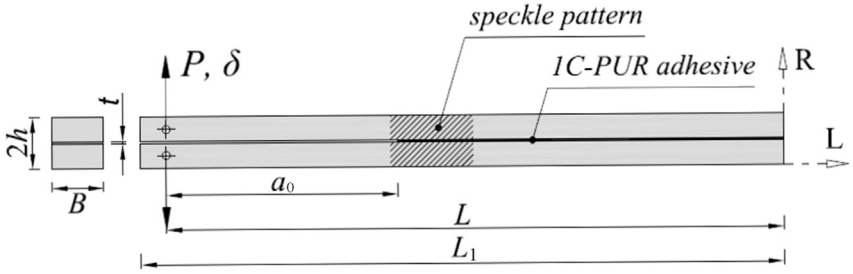

Fig. 1. DCB specimen geometry. Nominal dimensions are: $L_1 = 250$, $L = 240$, $2h = 20$, $B = 20$ and $t = 0.1$; units: mm.

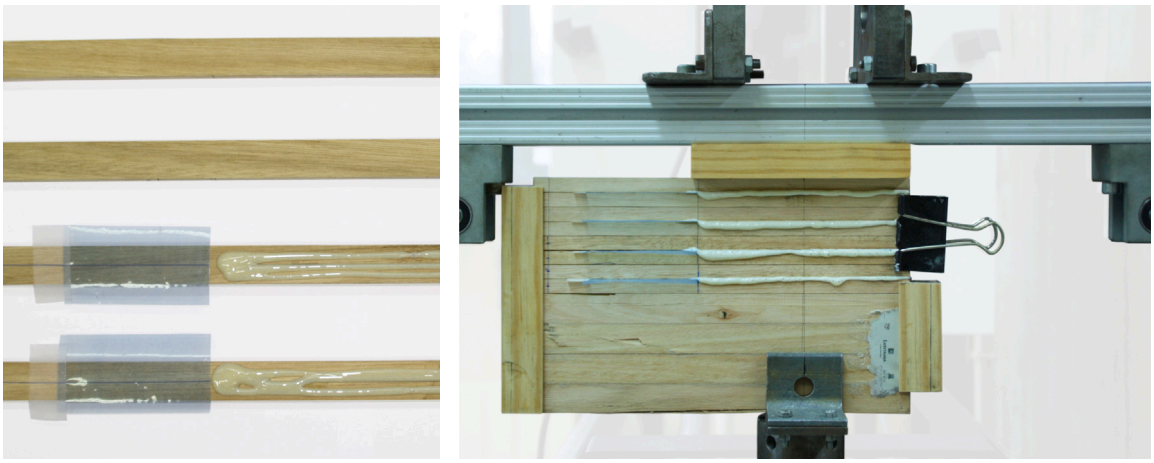

(a) (b)

Fig. 2. (a) Application of the adhesive on two DCB specimens; (b) application of pressure in the bonding process of four DCB specimens.

to the area of interest on the specimen surface to be recorded using an airbrush IWATA®, model CB-M. This ensured adequate grain size contrast and isotropy at the magnification scale. The image focus was guaranteed by setting a working distance of 103.5 ± 3 mm, yielding a conversion factor of 0.018 mm pixel^{-1}. For DIC analysis, image subsets of 15 × 15 pixels^2 size and 13 × 13 pixels^2 step were defined in a compromise between correlation and interpolation errors. The displacement resolution was in the range of 1–2×10^{-2} pixel (0.18–0.36 μm), estimated by performing a statistical analysis from measurements obtained by simple rigid-body translation tests [51,52]. The crack tip opening displacements of the DCB specimens, necessary to assess the cohesive law, were evaluated from a pair of imagen subsets located at the upper and lower part of the crack tip location. In the data procedure it was not necessary to measure the crack growth during the test, since the methodology is based on the Compliance Based Beam Method (CBBM) data reduction scheme to evaluate the $R-$curves [37].

3. Identification of cohesive laws

The CL defines the constitutive relationship between tractions and relative displacements allowing simulating progressive damage. Consequently, the accurate evaluation of this softening relationship (interfacial tractions versus separations) is relevant in the context of fracture characterization of materials. The identification of the CL under mode I loading using the Double Cantilever Beam (DCB) test (Fig. 1) for wood bonded joints was performed by three different approaches: a direct and two inverse methods. The direct one requires experimental measurement of the load–displacement data and crack tip opening displacement during the test. The inverse methods integrate finite element analyses including CZM with an optimization technique pointing to the minimization of the differences between numerical and experimental data.

3.1. Direct method

The attainment of the CL ($\sigma_I - w_I$) is based on the relation between the strain energy release rate under mode I loading and the crack tip opening displacement, $G_I = f(w_I)$, measured experimentally during the DCB test and its differentiation [53],

$$G_I = \int_0^{w_I} \sigma_I(\overline{w}_I)\, d\overline{w}_I \quad \therefore \quad \text{CL}: \quad \sigma_I(w_I) = \frac{G_I}{w_I}, \tag{1}$$

where σ_I represents the traction and w_I is the corresponding relative displacement registered during the fracture test employing DIC. A crucial aspect of this procedure is the correct evaluation of the evolution of the strain energy release rate during the DCB test as a function of the crack opening displacement, measured perpendicular to the crack path mode propagation. The evaluation of the strain energy release rate was performed by the Compliance Based Beam Method (CBBM) [54]. The advantage is the fact that this method is based the specimen compliance and equivalent crack concept, therefore with no need to measure the crack length during the test. Considering the Timoshenko beam theory, the DCB specimen compliance can be written as [54],

$$C = \frac{8a^3}{E_L B h^3} + \frac{12a}{5BhG_{LR}} \tag{2}$$

where E_L and G_{LR} are the wood elastic properties and B, h are specimen dimensions (Fig. 1) and a the current crack length. Since wood reveals important scatter on its elastic properties, the longitudinal modulus E_L was determined by an iterative procedure based on fitting the numerical initial specimen stiffness to the experimental one. A typical value for the shear modulus G_{LR} = 1926 MPa [49] was used, since the finite element analysis has shown that specimen compliance and strain energy release rate are almost insensitive to this elastic property. The equivalent crack length as function of the specimen

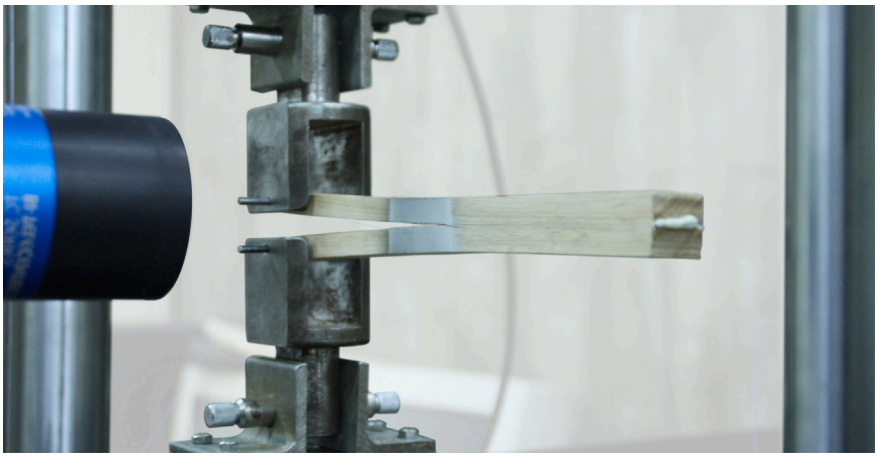

Fig. 3. DCB test set-up coupled with DIC.

compliance ($a_e = f(C)$) was achieved by solving Eq. (2), which yields the following relationship from the Irwin Kies expression,

$$G_I = \frac{P^2}{2B}\frac{dC}{da} = \frac{6P^2}{B^2 h}\left[\frac{2a_e^2}{E_L h^2} + \frac{1}{5G_{LR}}\right] \tag{3}$$

This approach provides the evolution of the strain energy release rate as a function of the equivalent crack length (also known as R–curve), which, in turn, was obtained during the test exclusively from the load–displacement data. Afterwards, the $G_I = f(w_I)$ relationship was obtained and a smoothing spline was adjusted to soften the noise before differentiation (Eq. (1)).

3.2. Inverse method

The inverse method consists of identifying the CL shape that minimizes the difference between numerical and experimental curves (dif $\approx$ 0, Fig. 4). In the present work, two approaches were tested and compared, so-called, the Global method and the Global–Local method. The Global method is based on the load *versus* displacement data (Fig. 4(a)), whilst the second one uses the load *versus* CTOD (w_I) measurements (Fig. 4(b)). The CBBM was applied in both, to determine the evolution of the strain energy. For the minimization of the difference between the experimental and numerical curves, a finite element model including a cohesive law with four linear softening segments was combined with an optimization algorithm.

In both methods, the developed algorithm requires the definition of five points over the experimental curves (Fig. 4). The first point is defined near the linear elastic limit and the last one corresponds to the maximum load. The remaining points are distributed between the first and last points, as illustrated, for instance, in the $P-\delta$ (Fig. 4(a)) or $P-w_I$ curves (Fig. 4(b)). Fig. 4(c) and Fig. 4(d) show the position of the corresponding points on the R–curve and on the resulting CL, respectively. The definition of the positions for each point i ($i = 2,\dots,5$) along the non-linear region of the curves ($P-\delta$ and $P-w$) establish the corresponding load (P_i), displacement (δ_i), crack opening displacement (w_i) and strain energy release rate ($G_{i-1:i}$).

3.2.1. Global based method

In this method, the stress value of each point can vary with no restrictions imposed by the remaining points. The first generation ($j = 1$) of the traction values corresponding to points 1–4 ($\sigma_i, i = 1,\dots,4$) is estimated assuming a randomly (σ_1) obtained from an acceptable interval for this material (5–15 MPa). The remaining traction values are estimated using the following restriction,

$$\sigma_i < \sigma_{i-1}, \quad i = 1,\dots,4 \tag{4}$$

and $\sigma_5 = 0$. The corresponding relative displacements ($w_i, i = 2,\dots,5$) can be determined using the strain energy release rate (Eq. (3)). Thus, this value of energy is equated to the area below the CL (Fig. 4(d)), thus allowing the definition of the corresponding relative displacement (w_i),

$$w_i = \frac{2G_{i-1:i}}{\sigma_{i-1}+\sigma_i} + w_{i-1}\ , \quad i = 2,\dots,5. \tag{5}$$

After this first iteration, the difference between the numerical and experimental curves is evaluated for each considered point,

$$\mathrm{dif}_i = P_i^{\mathrm{num}} - P_i^{\mathrm{exp}}\ , \quad i = 1,\dots,5. \tag{6}$$

The alterations of each estimated traction point are mutually independent. The stress values during the iterative process are estimated from the minimization the dif_i parameter.

It should be noted that stress value at a given point i influences the outline for the subsequent ones. Hence, the objective function used to estimate the stress values for the next iteration ($j+1$) have to include this effect into account. The experience shows that the relevance of the local stress value is progressive, which means that the load difference calculated in each point (Eq. (6)) is mostly dictated by the stress at this point. The influence of the neighbouring points depends on their sequential position, *i.e.*, the influence on point i of the point $i+2$ is inferior when compared with the one of point $i+1$. Considering this, a progressive weight factor (f_i) was implemented to estimate the stress value for the next generation,

$$\sigma_i^{j+1} = \sigma_i^j \left[\left(\frac{1}{n}\right)\sum_{i=1}^{5}\mathrm{dif}_i \cdot f_i\right] \quad i = 1,\dots,4\ ; \quad n = i-1 \tag{7}$$

with,

$$f_i = \frac{r^{i-1}}{\sum_i r^{i-1}}\ ; \quad r = b_f^{(n-1)} \ \wedge\ b_f = 0.4. \tag{8}$$

where the b_f parameter corresponds to a bias factor. The application of this factor results in a nonuniform distribution of weights in each local error (dif_i in Eq. (7)), that will affect the contribution of each error in the next estimated the stress value. The value of 0.4 was selected following a trial-and-error procedure.

Fig. 5 presents an organogram of the developed algorithm for the application of the proposed method. The process consists on the evaluation of the dif_i parameter for each point. When the dif_i parameter becomes negligible in a given point, the corresponding stress keeps the previous value and the analysis proceed. A convergent solution is found when all the points ($k = 4$ in this example) satisfy this requirement.

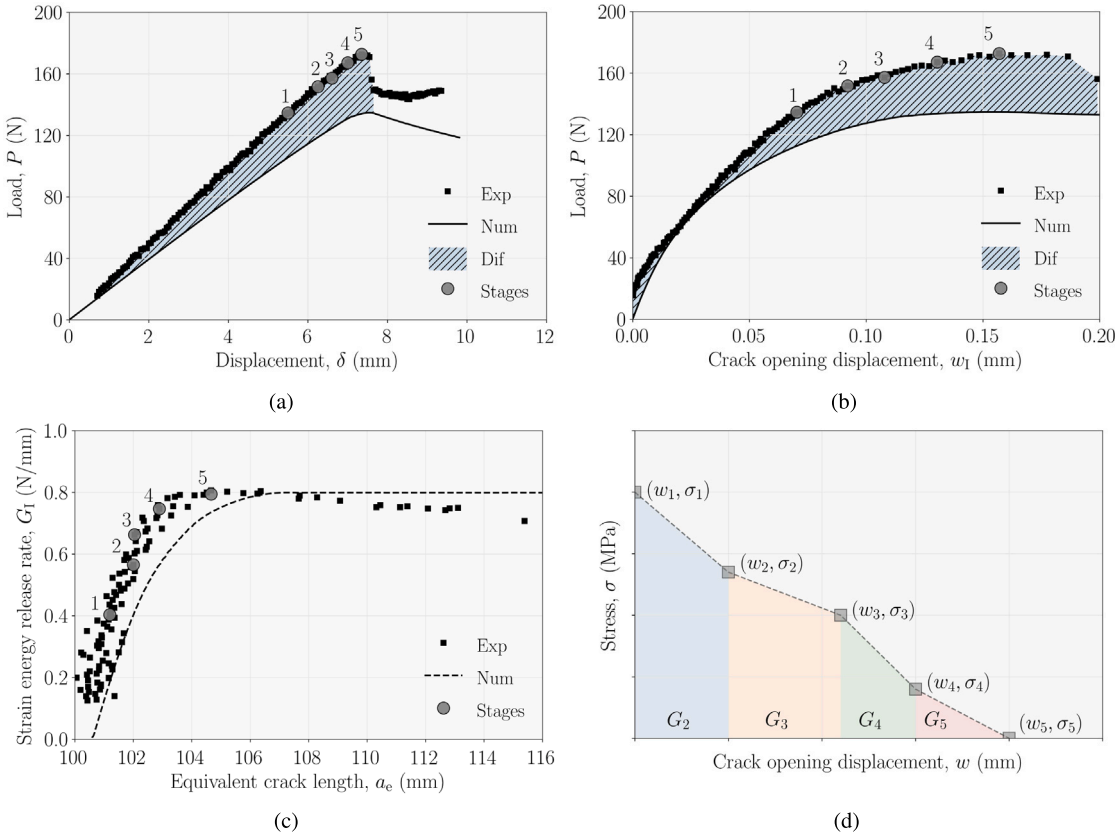

Fig. 4. (a) Load–displacement curve (Global method); (b) Load-w_I curve (Global–Local method); (c) R–curve; and (d) Cohesive law curve.

3.2.2. Global–local based method

The objective defined for this method was the minimization between a numerical and experimental load-w_I curve (Fig. 4(b)). Combining the crack opening distance ($w_{I,i}$) with the strain energy data ($G_{I,i}$) the entire cohesive law can be identified by estimate only the ultimate stress (σ_1). The stress values for the remaining points as a function of the ultimate stress can then be evaluated as,

$$\sigma_i = \frac{2G_i}{w_i - w_{i-1}} - \sigma_{i-1} \; ; \quad i = 2, \dots, 4 \quad \wedge \quad \sigma_5 = 0 \tag{9}$$

The minimization of the difference between the experimental and numerical load-w_I curves allows identification the cohesive law parameters. The organogram of the implemented algorithm can be visualized in Fig. 6. Since the problem only depends of one variable (σ_1) the estimation process at each iteration is simpler when compared with previous inverse method. If the calculated difference is negative, the stress value has to increase and vice versa. In our case, a perceptual factor of 5% is used to estimate the next stress value. If a negative difference is followed by a positive one, the estimated stress value for the next iteration will be the average of these two previous values.

4. Numerical model

A two-dimensional numerical model of the DCB test was developed. The model was made of 4500 solid plane stress 8-node elements, as schematically represented in Fig. 7. A total of 115 cohesive elements with 6 nodes were located at the specimen mid-height to govern the damage initiation and propagation between the two beams. Small increments (0.01 of the applied displacement on top beam) were used to ensure smooth damage propagation in the course of the loading process using the elastic properties presented in Table 1. Before any simulation the dimensions (a_0, h, B) were updated according to experimental measurements. The elastic longitudinal modulus was identified by adjusting of the numerical response to the stiffness of each experimental load–displacement curve.

5. Cohesive zone model

A cohesive zone model constituted by four linear branches to simulate the softening behaviour was considered. After damage onset, the constitutive relationship is defined by the following equation,

$$\sigma = (1 - d)kw \tag{10}$$

where k represents the interfacial stiffness and d the damage parameter ranging from zero (undamaged state) to one (complete failure).

Starting from the knowledge of the values (w_i, σ_i) for $i = 1, \dots, n-1$ using the iterative procedure above described, the ultimate relative displacement for $i = n(w_n)$ is obtained equating the fracture energy (G_{Ic}) to the area of the poly-linear softening relationship (Fig. 8),

$$G_i - G_{i-1} = \sum_{i=2}^{n} \frac{(\sigma_i + \sigma_{i-1})(w_i - w_{i-1})}{2} \tag{11}$$

The equations of the damage parameter on the several branches (linear segments in Fig. 8) are obtained equating the respective $\sigma_i = f(w_i)$, relation to Eq. (10) which gives,

$$d = 1 - \frac{1}{kw}\left[\frac{\sigma_i(w - w_{i-1}) + \sigma_{i-1}(w_i - w)}{w_i - w_{i-1}}\right] \quad \text{for} \quad w_{i-1} \le w \le w_i, \quad \text{with } i = 2, \dots, n \tag{12}$$

This relation defines the evolution of the damage parameter along the softening process according to the different relations ensuing for each segment.

6. Results and discussion

6.1. Strain energy release rate

Fig. 9 shows the load (P) values related to both the cross-head displacement (δ) of the testing device and the crack tip opening displacements (w_I) measured by DIC, resulting from the experimental

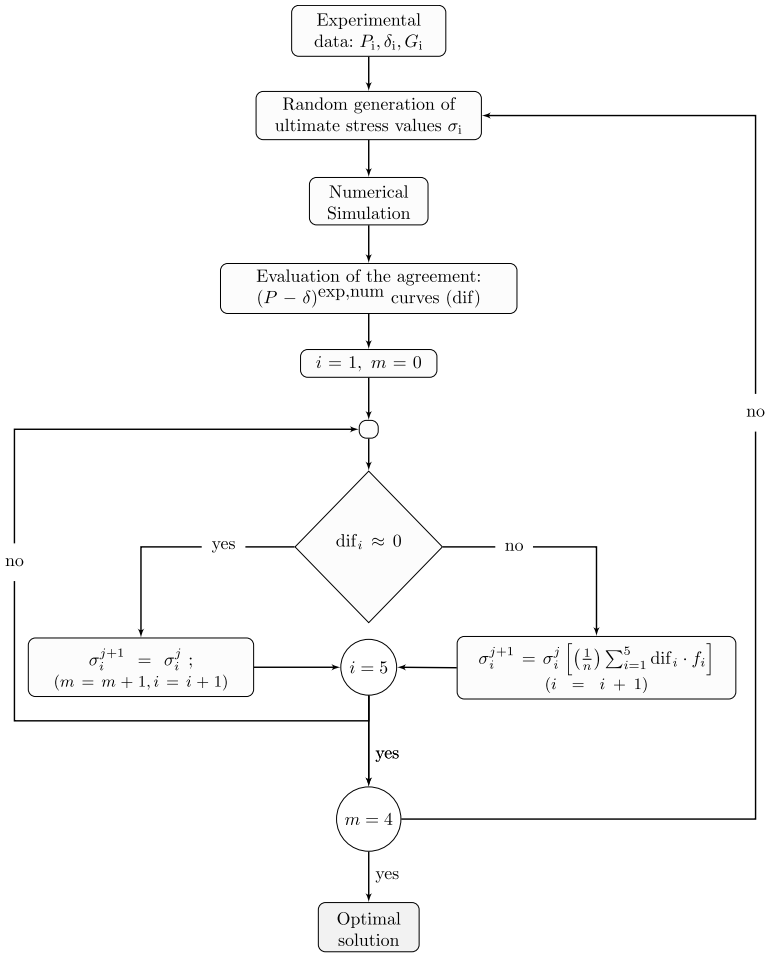

Fig. 5. Organogram of the developed algorithm for the Global based Method.

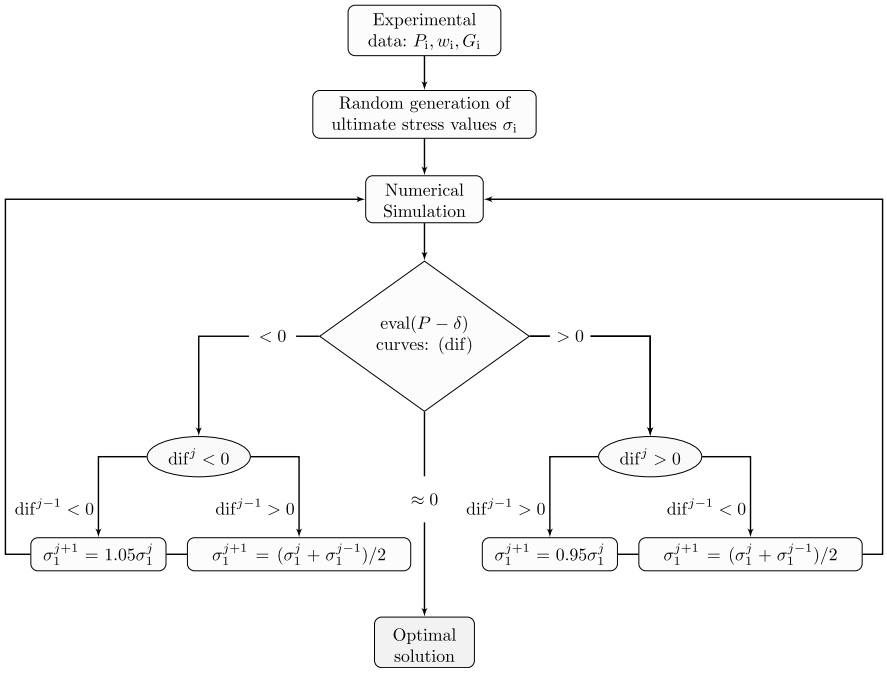

Fig. 6. Organogram of the developed algorithm for the Global–Local based method.

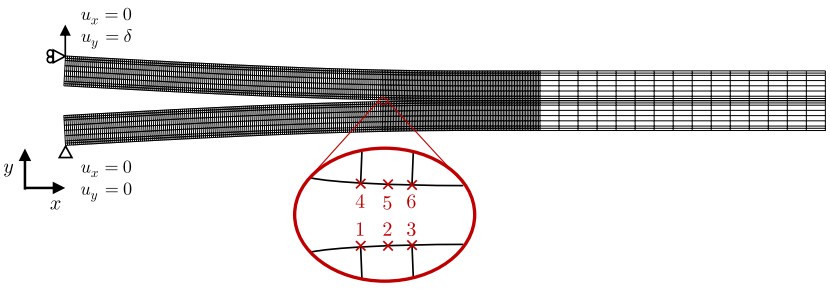

Fig. 7. Schematic representation of the DCB finite element mesh, with cohesive element positioning magnified.

Table 1
Elastic properties used in the numerical simulations of *Eucalyptus globulus* L..

E_L [GPa]	E_R [GPa]	E_T [GPa]	ν_{LR}	ν_{LT}	ν_{RT}	G_{LR} [GPa]	G_{LT} [GPa]	G_{RT} [GPa]
12–18	1.82	0.82	0.45	0.61	0.63	1.93	0.97	0.53

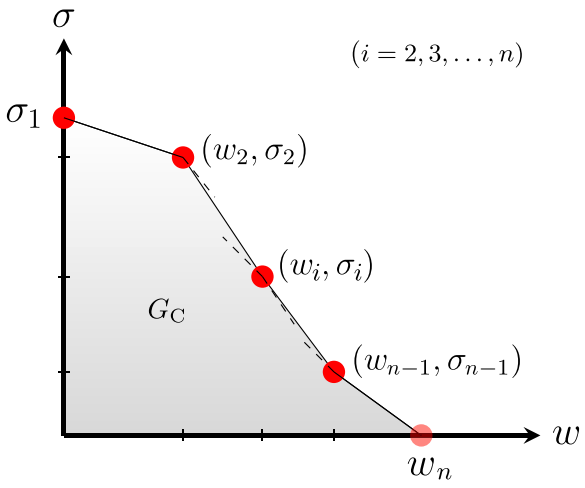

Fig. 8. Cohesive law with several linear branches.

tests on *Eucalyptus globulus* L. bonded specimens (solid lines), as well as counterpart numerical curves (dashed lines). The latter curves are obtained by adjusting a numerical model using global (Fig. 9(a)) and global–local (Fig. 9(b)) inverse method approaches. As can be seen, the results are consistent.

The corresponding R−curves obtained by means of the described CBBM are shown in Fig. 10. These curves reveal two main branches; an initial continuously increasing trend representative of the fracture process zone (FPZ) development that is followed by an almost constant region characteristic of the self-similar crack growth phenomenon and so defines the value of critical strain energy release rate (G_{Ic}), *i.e.*, the material's toughness to crack-growth. The zig-zag phenomenon observed essentially in the firs branch of the R-curves result from noise visible in the load–displacement curves that is amplified due to compliance differentiation (Eq. (3)). As can be seen, most of the curves showed plateaus for considerable crack extent, which means that the FPZ was fully developed. The value of G_{Ic} over the horizontal asymptote was calculated from each curve as summarised in Table 2, giving an average experimental value of 0.73 N/mm. Moreover, Table 2 reports the output parameters of applying the CBBM method: E_f, P_{max}, C_0, and $G_{I,Pmax}$. As it can be noticed, as the difference between G_{Ic} and $G_{I,Pmax}$ is minimal, the latter can be taken as a practical measure of the critical strain energy release rate in mode I.

The reported mean value of G_{Ic} for *Eucalyptus globulus* L. specimens bonded with 1C-PUR is considerably higher compared to DCB bonded joints using other species as adherents. In particular, an average fracture energy of 0.241 N/mm was reported in [32] for spruce wood bonded using 1C-PUR (Purbond HB S309) with five different spreading quantities and applying the direct compliance method (with crack propagation measurements) according to [30]. In the case of spruce with fibre-reinforced PUR adhesive studied by [55], an average specific fracture energy of 0.44 N/mm was obtained by also applying the direct compliance method.

Focusing on research that has used the same data reduction method as the one applied in the present work (CBBM), it follows that DCB eucalyptus bonded joints with 1C-PUR also lead to higher G_{Ic} values than those resulting from DCB bonded joints of *Pinus pinaster Ait* and epoxy adhesive (Araldite 2015) [33,36]. Specifically, a mean G_{Ic} value of 0.34 N/mm was obtained by [33], while a range between approximately 0.5 and 0.55 N/mm was reported in [36], although the latter with a low number of tests. A mean G_{Ic} value of 0.31 N/mm was obtained from DCB specimens of *Pinus pinaster Ait* solid wood applying the same CBBM in [37], showing the small difference compared to glued joints also in this species. To the author's knowledge, there are no studies on wood bonded joints using 1C-PUR adhesive and the CBBM as a data reduction scheme.

The failure of the adhesive joint specimens typically occurred cohesively, i.e., within the adhesive layer. Post-mortem analysis of the tested specimens revealed that a thin pellicle of adhesive was typically present on both adherents failure surfaces.

6.2. Cohesive law identification

For the identification of the cohesive laws of *Eucalyptus globulus* L. bonded joints with 1C-PUR adhesive applying the direct method, the CTOD values were monitored during the test in order to establish the $G_I = f(w_I)$. Subsequently, splines functions were adjusted to allow differentiation (Eq. (1)) and identification of the CL. The obtained CL (Fig. 11(a)) reveal some difficulty to capture with rigour the maximum local traction owing to inaccuracies characteristic of the early stage of the curves.

The two inverse procedures were also applied to the ensemble of the experimental data. The global based method can be sensible to any spurious variations of the specimen compliance, but it reveals to be quite easy to implement and execute. In fact, it does not require any specific equipment (*e.g.*, DIC) to monitor CTOD, as occurs in the direct method. Fig. 11(b) shows the CLs obtained by this method taking into account the quality of results adjustment regarding numerical versus experimental load–displacement curves (Fig. 9). It can be stated that CL shapes are more uniform and point to less scatter on the local strength when compared with the ones ensuing from the direct method. In order to minimize the influence of spurious compliance variations on the resulting CLs, a global–local procedure was also applied to the experimental $P - w_I$ curves, whose numerical versus experimental

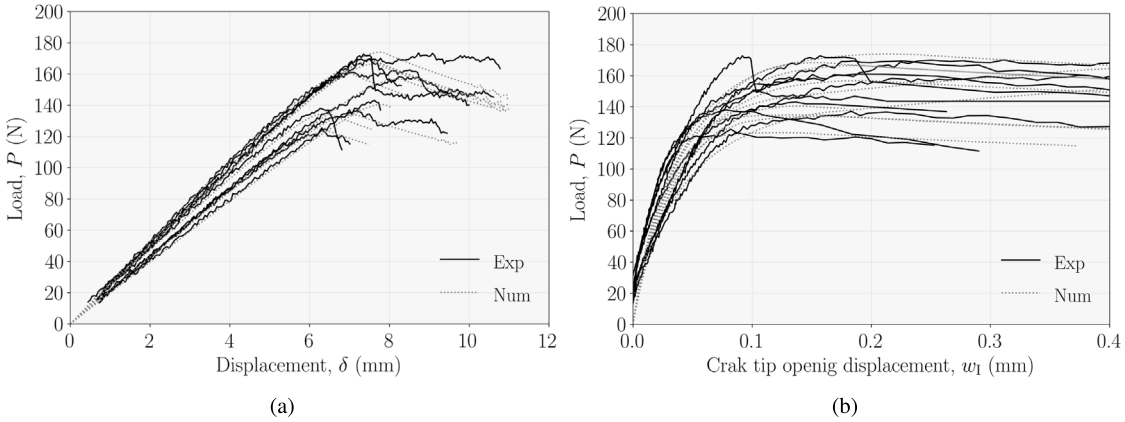

Fig. 9. (a) load–displacement experimental and numerical curves; (b) load-crack tip opening displacement experimental and numerical curves.

Table 2
Fracture parameters and cohesive law identification by direct and inverse methods.

Specimen	E_f	P_{max}	C_0	$G_{I,Pmax}$	G_{Ic}	Direct		Global based		Global–Local based	
						σ_I^{max}	w_{Ic}	σ_I^{max}	w_{Ic}	σ_I^{max}	w_{Ic}
	[MPa]	[N]	[mm/N]	[N/mm]	[N/mm]	[MPa]	[mm]	[MPa]	[mm]	[MPa]	[mm]
1	16844	173.51	0.039	0.92	0.81	9.36	0.32	10.73	0.17	10.55	0.23
2	16967	162.62	0.039	0.83	0.74	8.34	0.39	11.80	0.17	9.69	0.17
3	14305	166.26	0.046	0.90	0.86	9.65	0.17	13.03	0.16	11.72	0.13
4	14436	158.24	0.046	0.83	0.85	6.76	0.29	11.29	0.20	10.20	0.22
5	13679	137.12	0.046	0.62	0.61	5.83	0.24	9.01	0.19	10.20	0.16
6	15806	137.96	0.043	0.57	0.57	10.84	0.10	8.76	0.16	10.28	0.11
7	13162	125.51	0.048	0.53	0.51	11.47	0.17	10.90	0.14	10.71	0.11
8	12384	143.03	0.051	0.72	0.72	7.79	0.14	15.10	0.14	9.79	0.16
9	15999	172.74	0.041	0.83	0.83	8.23	0.18	12.51	0.16	9.79	0.19
10	15427	169.57	0.042	0.84	0.81	8.07	0.23	10.82	0.20	10.20	0.22
Mean	14901	154.66	0.044	0.76	0.73	8.55	0.21	11.47	0.17	10.31	0.17
SD	1555	17.28	0.004	0.14	0.13	1.821	0.087	1.968	0.023	0.627	0.045
CoV (%)	10.4	11.2	9.1	18.7	17.2	21.3	40.9	17.2	13.3	6.1	26.9

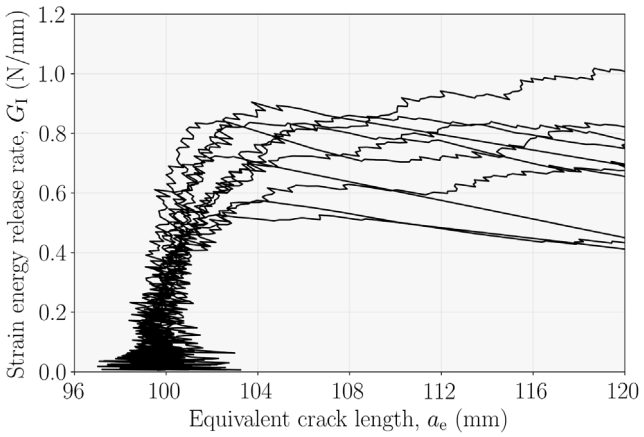

Fig. 10. Experimental R-curves.

adjustment can be visualized in Fig. 11(c). In fact, the existence of a local information (CTOD measured at the crack tip) allows to overcome some inaccuracies intrinsic to global method based on structural specimen response. The resulting CLs do not differ markedly from the ones ensuing from the global based method. In fact, the local strengths and ultimate opening displacement at the crack tip are of the same order of magnitude. The identified parameters from the direct and the global and global–local inverse methods are summarised in Table 2.

For the sake of a better comparison, the average CLs were plotted in the same graph (Fig. 11(d)). It can be settled that the local strength resulting from the direct method is not in agreement with the remaining cases. This is explained by the difficulties of the performed experimental measurements in the early stages of the $G_I = f(w_I)$ curve. The remaining global profile of the softening region is quite similar for the three average CLs.

7. Conclusions

In this work, three different methods have been used to identify the cohesive laws representative of mode I fracture behaviour of *Eucalyptus globulus* Labill bonded joints.

A direct method based on local measurement of crack tip displacements using DIC gives rise to cohesive laws with some inconsistencies on the local strength evaluation. This difficulty was explained by inaccurate assessment of the opening displacements at crack vicinity in the early stages loading using DIC which make difficult to assess the $G_I = f(w_I)$ curves at those stages.

In addition, two inverse based procedures were applied. The global approach lies of fitting numerically the experimental load–displacement curve by successive iterations involving alteration of the adopted cohesive law. In order to be less sensitive to spurious variation of specimen compliance, a global–local method was also developed. In this case, the applied load, as a global parameter, was combined with a local measurement of the crack tip opening displacement (w_I). The cohesive laws ensuing from these two methods point to local strength, ultimate crack opening displacement and global profile in close agreement. This statement leads to the conclusion that the global inverse method is attractive taking into consideration its intrinsic simplicity.

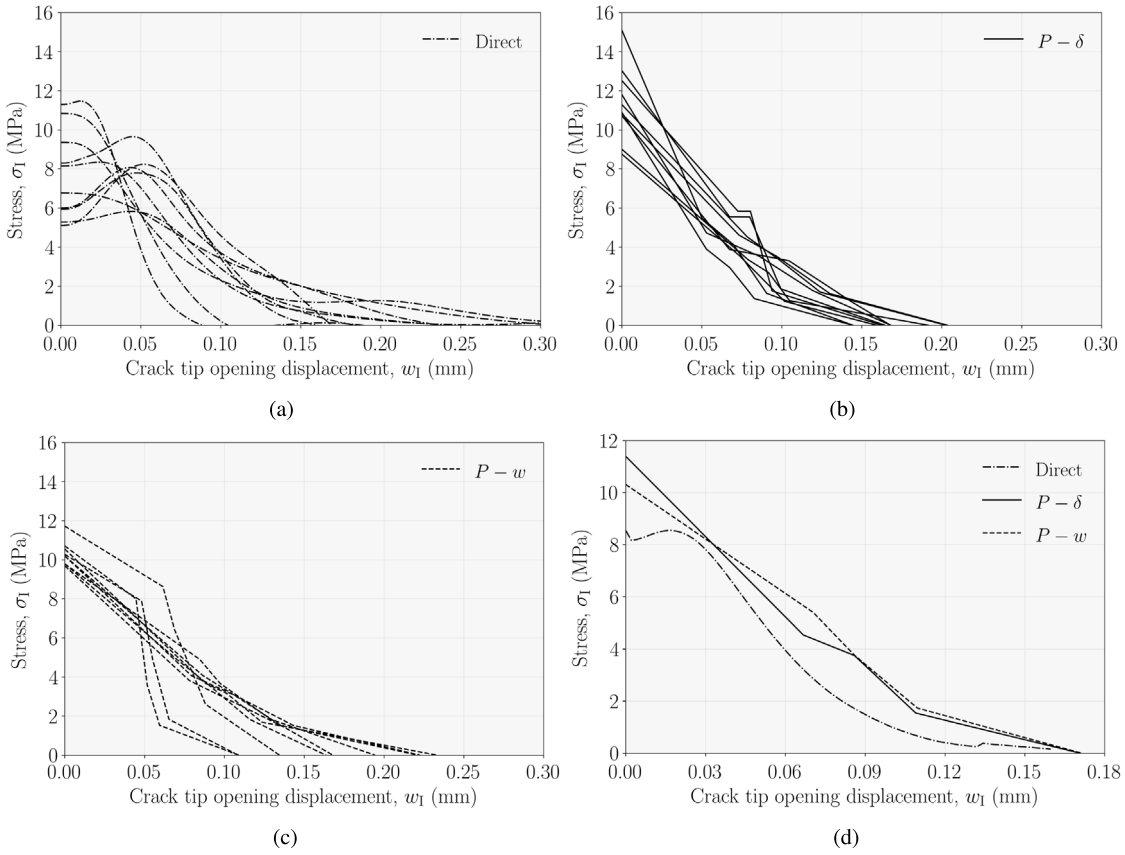

Fig. 11. Identification of cohesive laws: (a) direct method; (b) global-based method; (c) global–local based method; (d) Average.

CRediT authorship contribution statement

A. Majano-Majano: Conceptualization, Data curation, Formal analysis, Investigation, Methodology, Resources, Software, Validation, Visualization, Writing – original draft, Writing – review & editing. **A.J. Lara-Bocanegra:** Conceptualization, Data curation, Formal analysis, Funding acquisition, Investigation, Methodology, Resources, Software, Validation,Visualization, Writing – original draft, Writing – review & editing. **F. Pereira:** Data curation, Formal analysis, Investigation, Methodology, Resources, Software, Validation, Visualization, Writing – original draft, Writing – review & editing. **J. Xavier:** Conceptualization, Data curation, Formal analysis, Funding acquisition, Investigation, Methodology, Project administration, Resources, Software, Supervision, Validation, Visualization,Writing – original draft,Writing – review & editing. **J. Morais:** Conceptualization, Formal analysis, Funding acquisition, Investigation, Methodology, Project administration, Resources, Supervision, Validation, Writing – review & editing. **M.F.S.F. de Moura:** Formal analysis, Investigation, Methodology, Resource, Softwares, Supervision, Validation, Visualization,Writing – original draft, Writing – review & editing.

Declaration of competing interest

The authors declare the following financial interests/personal relationships which may be considered as potential competing interests: Jose Manuel Cardoso Xavier reports financial support was provided by NOVA University of Lisbon Faculty of Science and Technology. Jose Manuel Cardoso Xavier reports a relationship with NOVA University of Lisbon Faculty of Science and Technology that includes: employment.

Data availability

Data will be made available on request.

Acknowledgements

The work is part of the R&D&I Project PID2020-112954RA-I00 funded by MCIN/AEI/10.13039/501100011033. The authors acknowledge the Portuguese Foundation for Science and Technology (FCT) for the financial support associated to "Laboratório Associado de Energia, Transportes e Aeronáutica" (LAETA) by the project UID/EEA/04436/2019, and UNIDEMI by the project UIDB/00667/2020.

References

[1] Van Acker J. Opportunities and challenges for hardwood based engineered wood products. In: 9th Hardwood proceedings PT II. 2021.
[2] Aicher S, Christian Z, Dill-Langer G. Hardwood glulams - emerging timber products of superior mechanical properties. In: Proceedings of the world conference on timber engineering. 2014.
[3] Knorz M, van de Kuilen J-W. Development of a high-capacity engineered wood product - LVL made of European beech (Fagus sylvatica L.). In: Proceedings of the world conference on timber engineering. 2012.
[4] Tomé M, Almeida M, Barreiro S, Branco M, Deus E, Pinto G, et al. Opportunities and challenges of Eucalyptus plantations in Europe: the Iberian peninsula experience. Eur J For Res 2021;140(3):489–510.
[5] EN 1912:2012 Structural timber – Strength classes – Assignment of visual grades and species. CEN; 2012.
[6] Franke S, Marto J. Investigation of eucalyptus globulus wood for the use as an engineered material. In: Proceedings of the world conference on timber engineering. 2014.
[7] Crespo J, Majano-Majano A, Lara-Bocanegra A, Guaita M. Mechanical properties of small clear specimens of *Eucalyptus globulus* labill. Materials 2020;13(4):906.
[8] Derikvand M, Kotlarewski N, Lee M, Jiao H, Nolan G. Flexural and visual characteristics of fibre-managed plantation *Eucalyptus globulus* timber. Wood Mater Sci Eng 2018;15(3):172–81.
[9] Derikvand M, Jiao H, Kotlarewski N, Lee M, Chan A, Nolan G. Bending performance of nail-laminated timber constructed of fast-grown plantation eucalypt. Eur J Wood Wood Prod 2019;77(3):421–37.
[10] Pangh H, Hosseinabadi H, Kotlarewski N, Moradpour P, Lee M, Nolan G. Flexural performance of cross-laminated timber constructed from fibre-managed plantation eucalyptus. Constr Build Mater 2019;208:535–42.

[11] Lara-Bocanegra A, Roig A, Majano-Majano A, Guaita M. Innovative design and construction of a permanent elastic timber gridshell. Proc Inst Civ Eng Struct Build 2020;173(5):352–62.
[12] Lara-Bocanegra A, Majano-Majano A, Ortiz J, Guaita M. Structural analysis and form-finding of triaxial elastic timber gridshells considering interlayer slips: Numerical modelling and full-scale test. Appl Sci 2022;12(11):5335.
[13] Majano-Majano A, Lara-Bocanegra A, Xavier J, Guaita M. Splitting capacity of Eucalyptus globulus beams loaded perpendicular to the grain by connections. Mater Struct 2022;55(5):147.
[14] Lehringer C, Gabriel J. Review of recent research activities on one-component PUR-adhesives for engineered wood products. In: Materials and joints in timber structures. Springer Netherlands; 2014, p. 405–20.
[15] Schmidt M, Glos P, Wegener G. Verklebung von Buchenholz für tragende Holzbauteile. Eur J Wood Wood Prod 2009;68(1):43–57.
[16] Brandmair A, Clauß S, PhHaß P, Niemz P. Verklebung von Laubhölzern mit 1K-PUR-Klebstoffen für den Holzbau. Bauphysik 2012;34(5):210–6.
[17] ETA-13/0642 VIGAM - Glued laminated timber of oak. Elaborados y Fabricados Gamiz S.A., Spain. Österreichisches Institut für Bautechnik (ÖIB); 2018.
[18] Z-9.1-679 BS-Holz aus Buche und BS-Holz Buche-Hybridträger und zugehörige Bauarten. Studiengemeinschaft Holzleimbau e.V., Germany. Deutsches Institut für Bautechnik (DIBt); 2019.
[19] López-Suevos F, Richter K. Hydroxymethylated resorcinol (HMR) and novolak-based HMR (n-HMR) primers to enhance bond durability of eucalyptus globulus glulams. J Adhes Sci Technol 2009;23(15):1925–37.
[20] Martins C, Dias A, Cruz H. Blue gum: assessment of its potential for glued laminated timber beams. Eur J Wood Wood Prod 2020;78(5):905–13.
[21] Lara-Bocanegra A, Majano-Majano A, Crespo J, Guaita M. Finger-jointed eucalyptus globulus with 1C-PUR adhesive for high performance engineered laminated products. Constr Build Mater 2017;135:529–37.
[22] Lara-Bocanegra A, Majano-Majano A, Arriaga F, Guaita M. Eucalyptus globulus finger jointed solid timber and glued laminated timber with superior mechanical properties: Characterisation and application in strained gridshells. Constr Build Mater 2020;265:120355.
[23] EN 14080:2013 Timber structures. Glued laminated timber and glued solid timber. Requirements. CEN; 2013.
[24] EN 302-1:2013 Adhesives for load-bearing timber structures. Test methods. Part 1: Determination of longitudinal tensile shear strength. CEN; 2013.
[25] Sterley M, Serrano E, Enquist B. Fracture characterisation of green-glued polyurethane adhesive bonds in Mode I. Mater Struct 2013;46(3):421–34.
[26] Alfano G. On the influence of the shape of the interface law on the application of cohesive-zone models. Compos Sci Technol 2006;66(6):723–30.
[27] Campilho R, Banea M, Neto J, da Silva L. Modelling adhesive joints with cohesive zone models: effect of the cohesive law shape of the adhesive layer. Int J Adhes Adhes 2013;44:48–56.
[28] Fernández-Cañadas L, Iváñez I, Sanchez-Saez S. Influence of the cohesive law shape on the composite adhesively-bonded patch repair behaviour. Composites B 2016;91:414–21.
[29] Pereira F, Dourado N, Morais J, de Moura M. A new method for the identification of cohesive laws under pure loading modes. Eng Fract Mech 2022;271:108594.
[30] Gagliano J, Frazier C. Improvements in the fracture cleavage testing of adhesively-bonded wood. Wood Fiber Sci 2001;33(3):377–85.
[31] Lavisci P, Pizzo B, Gagliano J, Triboulot P, De Ciechi M. Fracture energy testing of thick joints with structural wood adhesives. Holz Als Roh- Und Werkstoff 2003;61(5):355–7.
[32] Veigel S, Follrich J, Gindl-Altmutter W, Müller U. Comparison of fracture energy testing by means of double cantilever beam-(DCB)-specimens and lap joint testing method for the characterization of adhesively bonded wood. Eur J Wood Wood Prod 2012;70(1–3):3–10.
[33] Xavier J, Morais J, Dourado N, de Moura MFSF. Measurement of mode I and mode II fracture properties of wood-bonded joints. J Adhes Sci Technol 2011;25(20):2881–95.
[34] Andersson T, Biel A. On the effective constitutive properties of a thin adhesive layer loaded in peel. Int J Fract 2006;141(1–2):227–46.
[35] Valoroso N, Sessa S, Lepore M, Cricrì G. Identification of mode-I cohesive parameters for bonded interfaces based on DCB test. Eng Fract Mech 2013;104:56–79.
[36] Silva F, Xavier J, Pereira F, Morais J, Dourado N, Moura M. Determination of cohesive laws in wood bonded joints under mode I loading using the DCB test. Holzforschung 2013;67(8):913–22.
[37] Xavier J, Oliveira M, Monteiro P, Morais J, Moura M. Direct evaluation of cohesive law in mode I of *Pinus pinaster* by digital image correlation. Exp Mech 2014;54(5):829–40.
[38] Majano-Majano A, Lara-Bocanegra A, Xavier J, Morais J. Measuring the cohesive law in mode I loading of *Eucalyptus globulus*. Materials 2019;12(1):23.
[39] Maier G, Bocciarelli M, Fedele R. Some innovative industrial prospects centered on inverse analyses. In: Mróz Z, Stavroulakis G, editors. Parameter identification of materials and structures. Springer Vienna; 2005, p. 55–93.
[40] Cox B, Yang Q. Cohesive zone models of localization and fracture in bone. Eng Fract Mech 2007;74(7):1079–92.
[41] Oh J-C, Kim H-G. Inverse estimation of cohesive zone laws from experimentally measured displacements for the quasi-static mode I fracture of PMMA. Eng Fract Mech 2013;99:118–31.
[42] Hong S, Kim K-S. Extraction of cohesive-zone laws from elastic far-fields of a cohesive crack tip: a field projection method. J Mech Phys Solids 2003;51(7):1267–86.
[43] Ferreira M, Venturini W, Hild F. On the analysis of notched concrete beams: From measurement with digital image correlation to identification with boundary element method of a cohesive model. Eng Fract Mech 2011;78(1):71–84.
[44] Affagard J-S, Mathieu F, Guimard J-M, Hild F. Identification method for the mixed mode interlaminar behavior of a thermoset composite using displacement field measurements and load data. Composites A 2016;91:238–49.
[45] Xu Y, Guo Y, Liang L, Liu Y, Wang X. A unified cohesive zone model for simulating adhesive failure of composite structures and its parameter identification. Compos Struct 2017;182:555–65.
[46] Majano-Majano A, Lara-Bocanegra A, Xavier J, Pereira F, Morais J. Direct evaluation of mode I cohesive law of eucalyptus bonded joints. Procedia Struct Integr 2022;37:492–9.
[47] Pereira F, de Moura M, Dourado N, Morais J, Xavier J, Dias M. Direct and inverse methods applied to the determination of mode I cohesive law of bovine cortical bone using the DCB test. Int J Solids Struct 2017;128:210–20.
[48] EN 408:2011+A1, Timber structures—Structural timber and glued laminated timber—Determination of some physical and mechanical properties. CEN; 2011.
[49] Crespo J, Aira J, Vázquez C, Guaita M. Comparative analysis of the elastic constants measured *via* conventional, ultrasound, and 3-D digital image correlation methods in *Eucalyptus globulus* labill. BioResources 2017;12(2):3728–43.
[50] ARAMIS. v.6.0.2 user's manual revision A. Braunschweig, Germany: GOM mbH; 2007.
[51] Xavier J, de Jesus A, Morais J, Pinto J. Stereovision measurements on evaluating the modulus of elasticity of wood by compression tests parallel to the grain. Constr Build Mater 2012;26(1):207–15.
[52] Jones E, Iadicola M, editors. A good practices guide for digital image correlation. Int Digit Imag Correl Soc 2018.
[53] Rice J. A path independent integral and the approximate analysis of strain concentration by notches and cracks. J Appl Mech 1968;35(2):379–86.
[54] de Moura M, Morais J, Dourado N. A new data reduction scheme for mode I wood fracture characterization using the double cantilever beam test. Eng Fract Mech 2008;75(13):3852–65.
[55] Harm M. Vergleich dreier Verfahren zur Bestimmung der Verklebefestigkeit von Vollholz [Master's thesis], Austria: Universität für Bodenkultur Wien; 2006.